

Supporting Information
for the
Article entitled

Femtosecond Excited State Dynamics and Nitric Oxide Photorelease in a
Prototypical Ruthenium Nitrosyl Complex

authored by

Vasily Vorobyev, Darya S. Budkina, Alexander N. Tarnovsky*

Department of Chemistry and the Center for Photochemical Sciences, Bowling Green State
University, Bowling Green, Ohio 43403, USA

CONTENT: METHODS AND RESULTS

Materials	SI3
Quantum chemical computations of vertical excitation transitions	SI3
Fig. 1SI. Absorption spectrum and EOM-CCSD excitation energies	SI4
Description of spectral deconvolution of the UV-vis absorption spectrum	SI5-6
Fig. 2SI. Deconvolution of the UV-vis absorption spectrum	SI7
Table 1SI. EOM-CCSD energies and oscillator strengths of transitions	SI8-9
Description of femtosecond transient absorption experiments	SI10-11
Fig. 3SI. Excitation energy dependence of 2- and 100-ps transient absorption	SI12
Fig. 4SI. Excitation energy dependence of long-time transient absorption	SI12
Fig. 5SI. Ultrafast processes involved and their time scales: a summary	SI13
Table 2SI. A summary of time constants from multiexponential fits	SI13
Fig. 6SI. Full set of ultrafast transient absorption spectra	SI14
Fig. 7SI. Transient absorption at 415 nm probe wavelength; different λ_{exc}	SI15
Fig. 8SI. Representative kinetic ΔA traces, 510 nm excitation	SI16
Fig. 9SI. Representative kinetic ΔA traces, 410 nm excitation	SI16
Fig. 10SI. Representative kinetic ΔA traces, 550 nm excitation	SI17

Fig. 11SI. UV ΔA kinetic traces; 340 nm excitation, TOPAS-probe	SI18
Fig. 12SI. Representative kinetic ΔA traces, 335 nm excitation	SI19
Fig. 13SI. Representative kinetic ΔA traces, 600 nm excitation	SI20
Fig. 14SI. Comparison of short-time ΔA spectra upon 340 and 510 nm excitation	SI21
Table 3SI. Vibrational coherences: a summary	SI22
Description of nanosecond transient absorption	SI23
Fig. 15SI. Product absorption spectra and their comparison	SI24
Evidence for NO photorelease upon 400 nm irradiation	SI25-26
Fig. 16SI. Steady-state photolysis spectra	SI25
Fig. 17SI. Solvation model of $[\text{RuNOCl}_5]^{2-}$	SI27
Table 4SI. Computed vibrational frequencies for ^1GS and $^3\pi_{\text{No}}^*$ $[\text{RuNOCl}_5]^{2-}$	SI28
Computational methodologies	SI29
References	SI30-31

Materials

The starting ruthenium compound was $\text{RuCl}_3 \cdot x\text{H}_2\text{O}$ from Oakwood Products, Inc.; ruthenium content was 37.8%. The studied complex, $\text{K}_2\text{RuNOCl}_5$ was synthesized as described in the literature.¹ The IR-spectrum and powder-XRD of the obtained compound are in agreement with the literature data.²⁻⁴ The absorption spectrum in water (Fig. 1SI) was constructed from the absorbance spectra measured for solutions of different dilution.

Deionized water was used to prepare the solutions. Aqueous solutions of $\text{K}_2\text{RuNOCl}_5$ are stable for several days in the dark. The signals of a hydrolysis product, *cis*- $\text{K}[\text{RuNO}(\text{H}_2\text{O})\text{Cl}_4]$, arouse in the ^{17}O , ^{99}Ru NMR spectra after 5 days of storing the solution at room temperature.¹

Quantum Chemical Computations of Vertical Excitation Transitions

The EOM-CCSD/PCM computations were carried out to evaluate the vertical electronic transitions of $[\text{RuNOCl}_5]^{2-}$ in aqueous solutions. The EOM-CCSD/PCM method suggests that the lowest-energy excitation ($^1A_2 \leftarrow ^1GS$) is predominantly metal-centered, $d_{xy} \rightarrow d_{x^2-y^2}$. The next excitation is of metal-to-ligand charge-transfer type, $d_{xy} \rightarrow \pi_{NO}^*$, corresponding to the $^1E \leftarrow ^1GS$ transition into a double-degenerate state. The $^1A_2 \leftarrow ^1GS$ and $^1E \leftarrow ^1GS$ transitions are predicted to be at 590 and 541 nm. The previous computational study⁵ on isolated $[\text{RuNOCl}_5]^{2-}$ came to a similar conclusion regarding the *d-d* and MCLT nature of the A_2 and E excited states. The corresponding transitions, $b_1 \rightarrow b_2(d_{xy} + p_\pi(Cl) \rightarrow d_{x^2-y^2})$ and $b_1 \rightarrow e(d_{xy} + p_\pi(Cl) \rightarrow d_\pi + p_\sigma(Cl))$ were computed to be 708 and 543 nm (CASSCF) and 692 and 590 nm (B3LYP). They differ within 0.35 eV from the EOM-CCSD/PCM transition energies of 590 and 541 nm and the values resulting from the spectral deconvolution of the absorption spectrum shown in Fig. 2SI (667 and 526 nm for seven Gaussian band fit, and 651 and 522 nm for the nine Gaussian band fit). These assignments add to early viewpoints, which were controversial.⁶ All other, higher-lying transitions are due to charge-transfer (CT) excitations, Table 1SI.

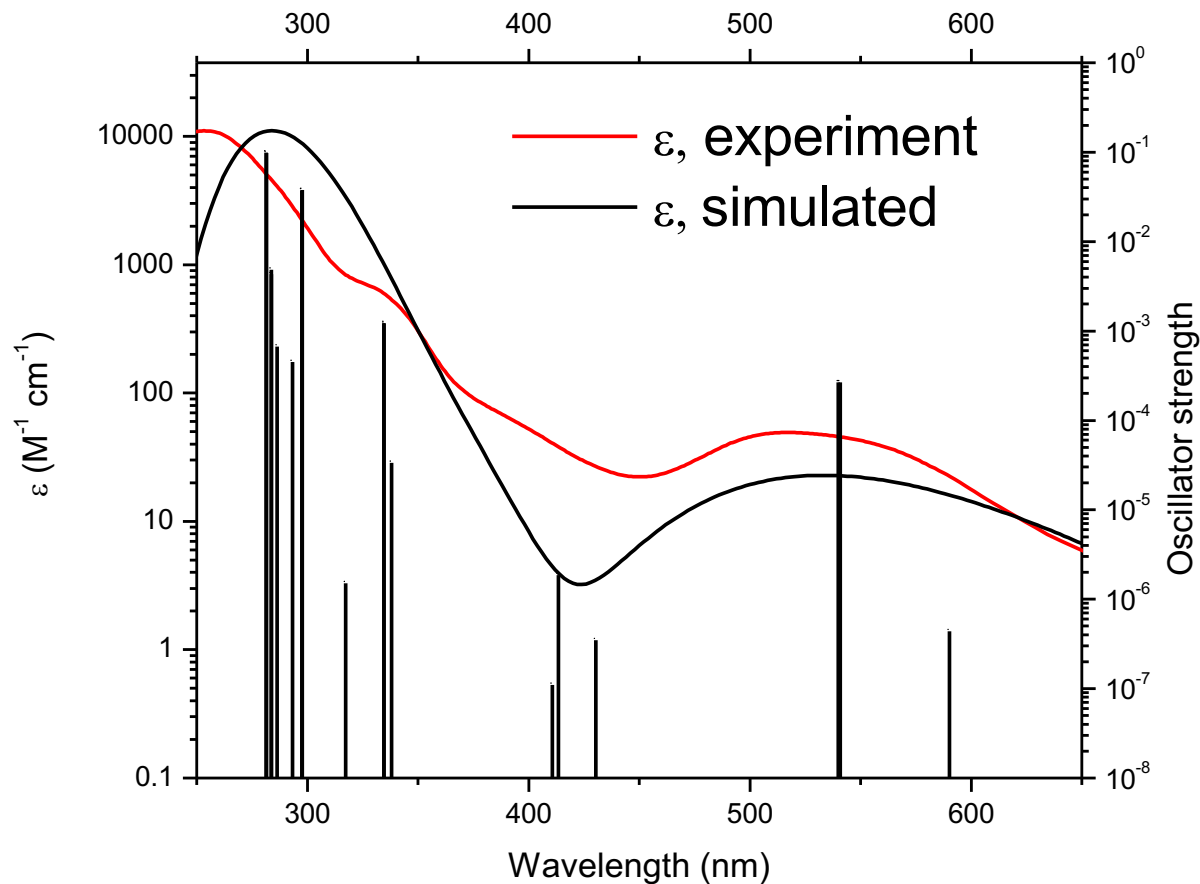


Fig. 1SI. The experimental steady-state absorption spectrum of RuNOCl_5^{2-} in water and the simulated spectrum based on EOM-CCSD/PCM computations of the vertical excitation transitions of the complex (note the logarithmic extinction scale). The vertical lines represent the computed oscillator strengths (right axis, plotted against the computed transition energies (see Table 1SI for the numerical values). For the qualitative comparison between the experimental and computed spectra, the computed transitions were broadened by 5060 cm^{-1} (fwhm).

Absorption Spectrum and Its Deconvolution

The absorbance of $[\text{RuNOCl}_5]^{2-}$ was measured in Spectrosil quartz cells of a different path length using a Varian Cary 50 Bio spectrophotometer and found to obey Lambert-Beer law in the range of concentrations from 0.25 M to 0.25 μM . The results of absorbance measurements performed with different concentration were used to construct the spectrum of the molecular decadic coefficient (ϵ) shown in Fig. 2SI.

The spectrum of the molecular decadic coefficient (ϵ) of $[\text{RuNOCl}_5]^{2-}$ plotted in the form ϵ/ν was deconvoluted using least-squares fitting into a sum of several Gaussian functions taken to represent individual electronic transitions. The spectrum deconvolution that used a sum of seven Gaussian functions yields the bands centered at 676, 521, 392, 327, 253, 212, and 192 nm, Fig. 2SI, Panel A). A total number of the transitions in the ultraviolet (UV) region is uncertain due to the broad nature of the absorption bands. To describe a very weak absorption in the long-wavelength part of the spectrum (above 620 nm), a 673-nm band was needed. We stress that, in view of the complexity of the spectrum, deconvolutions which would use a larger number of transitions or not to restrict an individual bandwidth to the one typical for vibronic spectra between the electronic excited states of polyatomic molecules in room-temperature liquids (2000–5000 cm^{-1}) are also possible. The fit shown in Fig. 2SIA reproduces the experimental spectrum satisfactorily using the smallest possible number (seven) of individual transitions.

For comparison, we also show the second-best fit that uses nine Gaussian functions, Fig. 2SIB. The corresponding transitions are centered at 651, 522, 359, 332, 275, 253, 234, 215, and 196 nm. It is apparent that in the seven-Gaussian fit the 394 nm band becomes blue shifted yielding the 359-nm band in the nine-Gaussian fit. The 328-nm band is somewhat broader than the 332 nm band. The 253 nm band is significantly broader, but only reaches a 389 nm wavelength with $\epsilon = 0.9 \text{ M}^{-1} \text{ cm}^{-1}$. Thus, in the seven-Gaussian fit, the 213 and 192 nm bands practically do not have any spectral overlap with excitation at 335 nm and longer wavelengths. In the nine-Gaussian fit, the 196, 215, and 234 nm bands have no overlap with the 335-nm wavelength.

The 253 nm band (seven-Gaussian fit) is broad and has a significant contribution at 335 nm ($\epsilon = 124 \text{ M}^{-1} \text{ cm}^{-1}$ vs. total $\epsilon = 596 \text{ M}^{-1} \text{ cm}^{-1}$ at this wavelength), whereas the contribution of the 253 nm band of the nine-Gaussian fit is negligibly small ($\epsilon < 0.4 \text{ M}^{-1} \text{ cm}^{-1}$ at 335 nm). Thus,

the 253, 327, and 392 nm bands in the seven-Gaussian fit contribute to the 335 nm absorbance in the ratio 124:404:2.9. In the nine-Gaussian description, the 253, 359, and 359 nm bands contribute to the 335 nm absorbance in the ratio 0.4:404:67. Upon 510 nm excitation, the contribution of the 394 and 332 nm bands seems not important (it is at most $1.2 \text{ M}^{-1} \text{ cm}^{-1}$ vs. the total $\varepsilon = 47 \text{ M}^{-1} \text{ cm}^{-1}$ at 510 nm). One can conclude that 510 nm (and 550 nm) excitation promotes the complex into the second excited state. Excitation at 675 nm is into the lowest excited state, but the contribution of the second transition (the 521 nm peak) may be important.

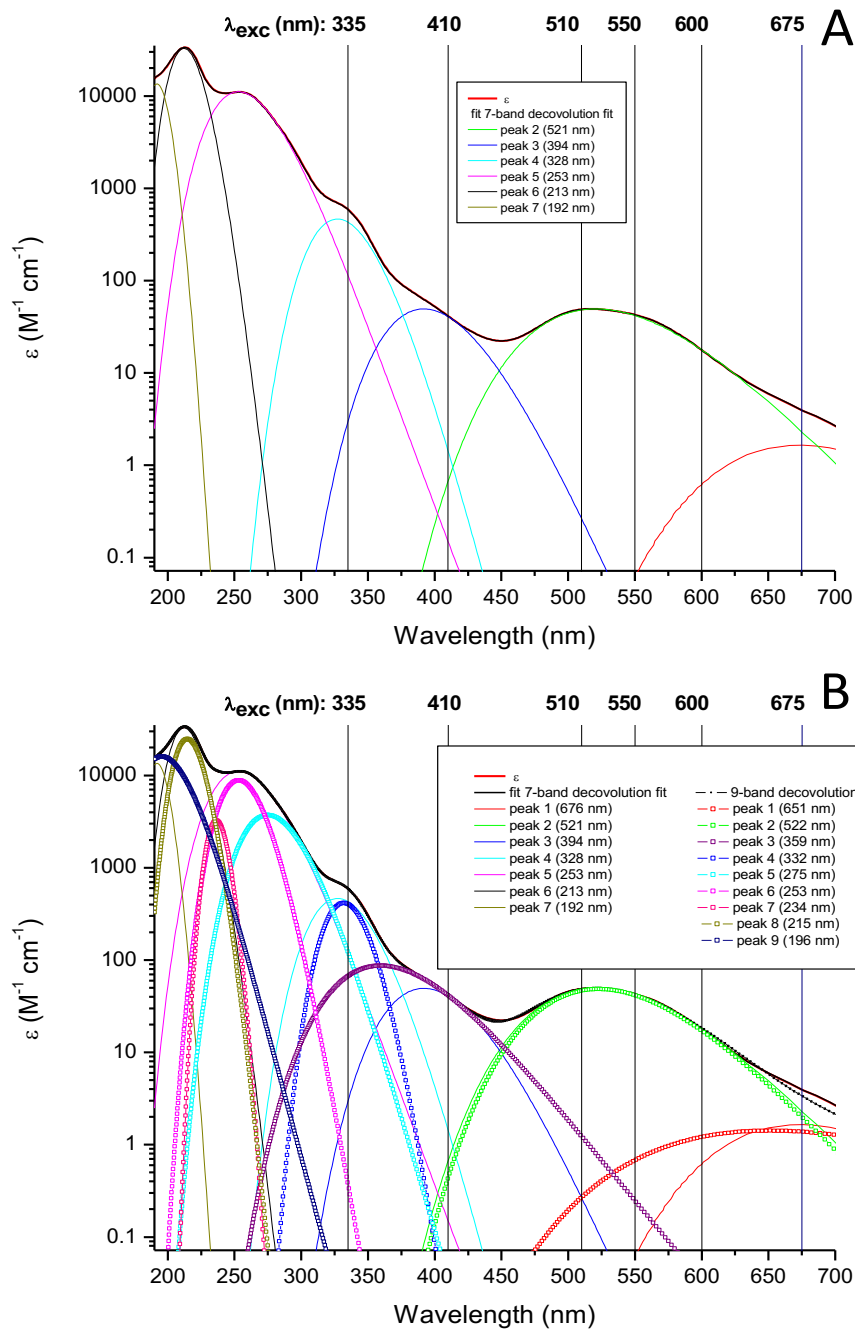
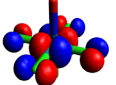
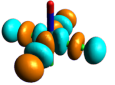
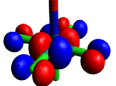

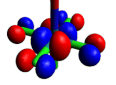
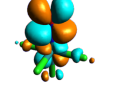
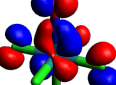

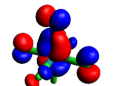

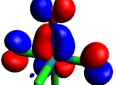
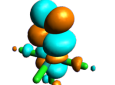
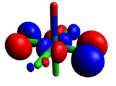
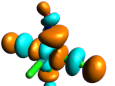
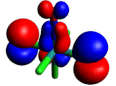
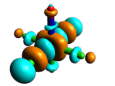
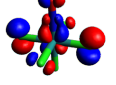
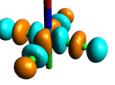
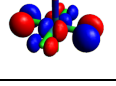
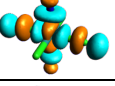
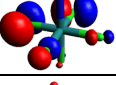
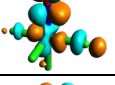
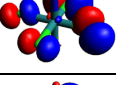
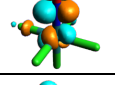
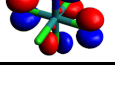
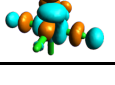
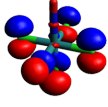
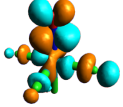
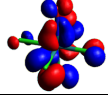
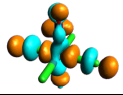

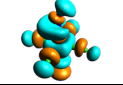
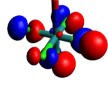
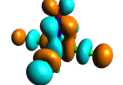
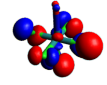



Fig. 2SI. The absorbance of RuNOCl_5^{2-} in water (plotted as the molecular decadic extinction coefficient, ϵ) and the deconvolution of the absorption spectrum into a sum of Gaussian-shaped bands taken to represent individual vibronic transitions. See the text for detail. Panel A: a fit that uses seven Gaussian functions with the peaks at 676, 521, 394, 328, 253, 213, and 192 nm. Panel B: a comparison of the seven-Gaussian fit with the second-best nine-Gaussian description (band maxima at 651, 522, 359, 332, 275, 253, 234, 215, and 196 nm). Vertical lines indicate the wavelengths used for excitation in the present femtosecond transient absorption experiments.

Table 1SI. Computed energies and oscillator strengths of first eighteen (N =1–18) vertical singlet electronic transitions for RuNOCl₅^{2- a)} in water by using the EOM-CCSD method with a PCM solvation model.

N	λ (nm)	Oscillator strength ^{b)}	Involved orbitals	Origin of the transferred electron density, weighted sum of the occupied MO c)	Destination of the transferred electron density, weighted sum of the occupied MO c)
1	590	$4.37 \cdot 10^{-7}$	$d_{xy} - p_{Cl} \rightarrow d_{x^2-y^2} - \sigma_{Cl}$		
2	541	$2.67 \cdot 10^{-4}$	$d_{xy} - p_{Cl} \rightarrow \pi_{NO}^* - d_{xz}$		
3	540	$2.67 \cdot 10^{-4}$	$d_{xy} - p_{Cl} \rightarrow \pi_{NO}^* - d_{xz}$		
4	430	$3.46 \cdot 10^{-7}$	$\pi_{NO}^* + d_{xz} - p_{Cl} \rightarrow \pi_{NO}^* - d_{yz}$		
5	414	$1.85 \cdot 10^{-6}$	$\pi_{NO}^* + d_{yz} - p_{Cl} \rightarrow \pi_{NO}^* - d_{xz}$		
6	411	$1.10 \cdot 10^{-7}$	$\pi_{NO}^* + d_{xz} - p_{Cl} \rightarrow \pi_{NO}^* - d_{yz}$		
7	338	$3.34 \cdot 10^{-5}$	$p_{Cl} \rightarrow d_{z^2} - \sigma_{Cl} - \sigma_{NO}$		
8	335	$1.21 \cdot 10^{-3}$	$p_{Cl} - \pi_{NO}^* - d_{xz} \rightarrow d_{x^2-y^2} - \sigma_{Cl}$		
9	335	$1.23 \cdot 10^{-3}$	$\pi_{NO}^* - p_{Cl} + d_{xz} \rightarrow d_{x^2-y^2} - \sigma_{Cl}$		
10	317	$1.51 \cdot 10^{-6}$	$p_{Cl} - d_{xy} \rightarrow d_{z^2} - \sigma_{Cl} - \sigma_{NO}$		
11	298	$3.76 \cdot 10^{-2}$	$p_{Cl} \rightarrow \pi_{NO}^* - d_{xz}$		
12	298	$3.73 \cdot 10^{-2}$	$p_{Cl} \rightarrow \pi_{NO}^* - d_{xz}$		
13	293	$4.48 \cdot 10^{-4}$	$p_{Cl} \rightarrow \pi_{NO}^* - d_{yz} - \sigma_{Cl}$		

14	286	$6.70 \cdot 10^{-4}$	$p_{Cl} \rightarrow \pi_{NO}^* - d_{xz}$		
15	284	$4.85 \cdot 10^{-3}$	$\pi_{NO}^* + d_{xz} - p_{Cl} \rightarrow d_{z^2} - \sigma_{Cl} - \sigma_{NO}$		
16	284	$4.30 \cdot 10^{-3}$	$\pi_{NO}^* + d_{xz} - p_{Cl} \rightarrow d_{z^2} - \sigma_{Cl} - \sigma_{NO}$		
17	282	$9.77 \cdot 10^{-2}$	$p_{Cl} \rightarrow \pi_{NO}^* + d_{x^2-y^2} - \sigma_{Cl}$		
18	281	$9.84 \cdot 10^{-2}$	$p_{Cl} \rightarrow \pi_{NO}^*$		

a) Optimized geometry using the BP86 density functional^{7,8} and the def2-TZVPP basis set.^{9,10}

b) Computed using the EOM-CCSD transition dipole moments and transition energies of the singlets.

c) For each N-transition, left and right figures correspond to a sum of molecular orbitals (weighed by their configuration interaction expansion coefficients) corresponding to an initial and a final electronic state connected by the transition. The occupied orbitals are shown in blue/red, and the virtual orbitals are shown in orange/cyan.

Femtosecond Transient Absorption

The samples were studied using two ultrafast transient absorption set-ups based on regeneratively amplified Ti:sapphire laser systems (Spectra-Physics) operating at a 1 kHz repetition rate. The output (35-fs (fwhm) 3.8 mJ pulses centered at 800 nm) of the laser system (Spitfire Pro) of the first set-up was 50:50 split. The first beam is sent to a TOPAS-C optical parametric amplifier (OPA, Light Conversion Lt.) to produce 335, 410, 510, 550, 600, and 675 nm excitation pulses. The second beam was delayed using a retroreflector mounted on a computer-controlled motorized translational stage to set a variable delay time with respect to the excitation pulse, attenuated and focused onto a 2-mm thick CaF₂ window to produce white-light continuum (wlc) probe pulses spanning the 340–770 nm range. The wlc beam was focused to a 75 μ m diameter spot at the sample and overlapped nearly collinearly (angle, 0.7°) with the excitation beam focused to a 150 μ m diameter spot. The laser system (Hurricane) of the second set-up, which was described previously,^{11,12} generates a train of 90 fs (fwhm) 0.9 mJ 800-nm pulses. The 50% split-off portion of the output was sent to a TOPAS OPA to generate 340 nm excitation pulses. The remaining part of the output was sent to either a variable time-delay stage, attenuated and focused onto a 4-mm thick CaF₂ window to generate a wlc probe light (340–780 nm), or another TOPAS OPA to produce tunable (290–390 nm) pulses, which were sent to the time-delay stage and used for probing. The excitation and probe beams were made to overlap at the sample position at a 6° angle, being 200 and 60 μ m in diameter.

In both set-ups, the excitation light, before being focused onto the sample, is sent through a Berek compensator to set the polarization plane to the magic angle (54.7°) with respect to that of the probe light and eliminate solute rotational signals, and through a mechanical chopper operating at a 500 Hz frequency. A fraction of the probe beam was split off before the sample to be utilized as a reference for the correction of the shot-to-shot pulse intensity fluctuations. The reference beam (made to bypass the sample) and the probe beam (after the sample) were dispersed by a spectrograph and recorded using matching photodiodes (TOPAS probe) or a dual CCD detector (wlc probe) synchronized to the 1 kHz repetition rate. The difference between the negative decadic logarithms of a probe-to-reference intensity ratio measured at a specific position of the optical stage for excitation on and off represents the change in the sample absorbance (ΔA) at the corresponding delay time. All experiments were performed at 294 K.

The solutions were circulated through a flow cell with a 0.2-mm path length to refresh the excited volume after each excitation shot. The RuNOCl_5^{2-} concentration of 0.13 M was used in the experiments utilizing excitation at 410 nm and longer wavelengths because of small ϵ coefficients of the complex at these wavelengths. In the experiments utilizing UV excitation the concentration used was 0.02 M when probing with the wlc light and 0.036 M when probing with the TOPAS light. The sample dynamics did not change with concentration, consistent with the absorbance of the sample obeying Lambert-Beer law in the wide concentration range ($0.25\text{--}0.25 \times 10^{-6}$ M). The ΔA signals depended linearly on excitation energy and the ΔA vs. excitation energy dependence passed through the origin, confirming that single-photon excitation is responsible for the measured data, Fig. 3,4SI. Typical excitation energy used was $200\text{--}350 \text{ nJ pulse}^{-1}$.

The ΔA signals from neat water were measured under the same excitation conditions and immediately after $[\text{RuNOCl}_5]^{2-}$ measurements. These signals, observed to be localized within $\sim 50\text{--}150$ fs around zero delay time, manifest the cross-phase modulation (xpm), stimulated Raman signals, and impulsive stimulated Raman scattering (ISRS),¹³⁻¹⁶ and the first two were used to correct ΔA data for group-velocity dispersion in the probe light. The water ΔA signals (after scaling to account for solute absorption at the excitation wavelength) were subtracted from the solution ΔA data to obtain the true ΔA data of $[\text{RuNOCl}_5]^{2-}$. In the experiments conducted using the 35-fs Spitfire-based set-up, the spectral width of the excitation pulses (600 cm^{-1}) gives a limit to the pulse duration of 25 fs. The ‘instantaneous’ part of the ΔA signal rise (360–390 nm probe) suggests the width (fwhm) of the pump-probe cross-correlation function (CCF) of 45 fs (λ_{exc} : 675, 600, and 550 nm), and 73 fs (λ_{exc} : 510, 410, and 335 nm) (under our condition of a fast chirp, the CCF width is equal to the excitation pulse duration¹⁴). The accuracy in our determination of the zero delay time is 10 fs (675, 600, and 550 nm) and 20 fs (510, 410 and 335 nm). In the TOPAS probe case, the water stimulated Raman emission signal (Fig. 11SI, 378–382 nm) represents the Gaussian-like CCF with the 98–110 fs width, yielding the 68–76 fs duration for excitation and probe pulses and the 20-fs accuracy in the zero delay time determination.

The recorded ΔA kinetic traces (typically, every 10 or 20 nm) were fitted to a sum of up to six exponential decay functions: $\sum_j a_j(\lambda) e^{-t/\tau_j}$, where $a_j(\lambda)$ is the amplitude and τ_j is the j -time constant. Time constants resulting from the single-point multiexponential fit analysis are summarized in Fig. 5SI and Table 2SI. Fit residuals $R(\lambda, t)$ were analyzed using fast Fourier transform (FFT) and exponentially damped cosine functions, Table 3SI.

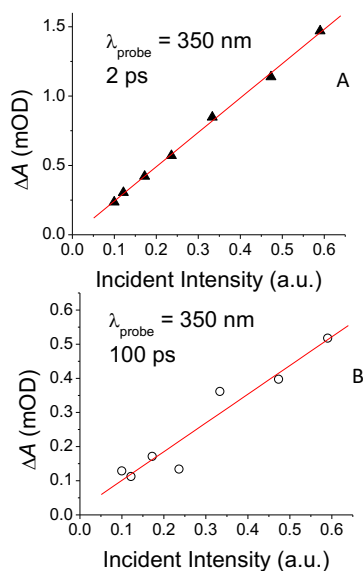


Fig. 3SI. Excitation energy dependence of transient absorption signals (symbols) following 340-nm excitation of $[\text{RuNOCl}_5]^{2-}$ (0.036 M) at the intermediate delay time of 2 ps (upper panel) compared to that of the signals measured at 100 ps delay time (bottom panel). The linear dependence of the signals with the excitation pulse energy is observed in both cases. Linear fits are shown as red lines. Note that 1 a.u. corresponds to $1.77 \mu\text{J pulse}^{-1}$.

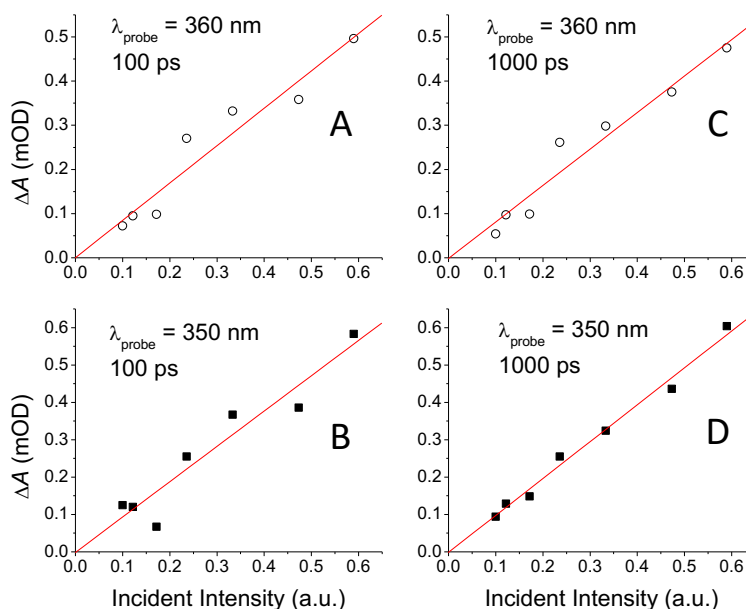


Fig. 4SI. Excitation energy dependence of transient absorption signals (symbols) is compared at long delay times of 100 and 1000 ps. 1 au corresponds to $1.77 \mu\text{J pulse}^{-1}$. The investigated probe wavelengths of 350 and 360 nm are indicative of the aquated product formation. Linear fits are shown as red lines. The linear dependence of the transient absorption signals with the excitation pulse energy is observed in both cases.

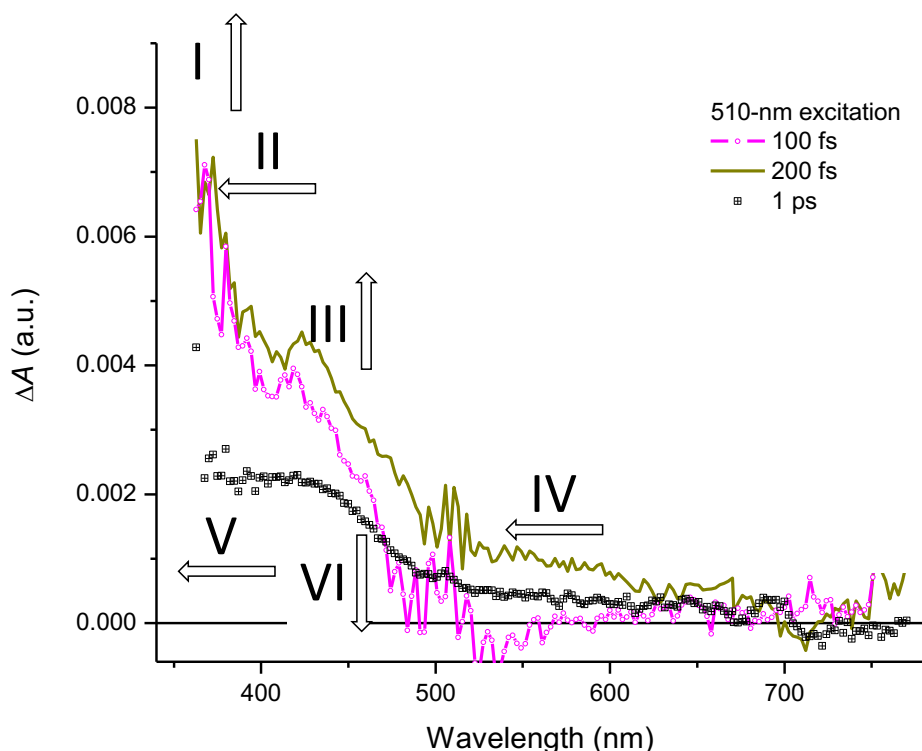


Fig. 5SI. The entire dynamics can be described using six major processes: rise of very hot ground-state absorption (I) and its relaxation (II), population of the $^3\pi_{NO}^*$ state (III), vibrational relaxation in the $^3\pi_{NO}^*$ state (IV) and at the bottom of the ground-state potential well (V), decay of the $^3\pi_{NO}^*$ state (VI), see Table 2SI for the derived time constants.

Table 2SI. Time constants resulting from multiexponential fit analysis of transient absorption kinetic traces measured for aqueous $[\text{RuNOCl}_5]^{2-}$.

	Excitation (nm)					
	675	600	550	510	410	335 ^{f)}
τ_I (fs) ^{a)}	-	~45	< τ_{II}	~50	< τ_{II}	~60
τ_{II} (fs) ^{b)}	-	95 ± 13	90 ± 20	~90	~100	80 ± 20
τ_{III} (fs) ^{c)}	observed at 80 fs (675 nm) and 90-120 fs (600 nm), Fig. 2B, main text		119 ± 13	120 ± 20	260 ± 60	210 ± 20
τ_{IV} (fs) ^{d)}	197 ± 21	316 ± 95	302 ± 82	~430	~500	520 ± 140
τ_V (fs) ^{e)}	205 ± 81	515 ± 122	506 ± 22	420 ± 60	820 ± 140	580 ± 140
τ_{VI} (ps)	3.2 ± 0.1					

Processes pronounced in the following spectral ranges (see also Fig. 5SI): rise^{a)} between 350 and 370 nm, decay^{b)} between 360 and 390 nm, 400–430 nm rise,^{c)} decay^{d)} from 450 to 600 nm, and decay^{e)} from 350 to 410 nm. ^{a)} τ_I is only an estimate and has not been resolved for 550 and 410 nm excitation; τ_I is estimated to be less than τ_{II} . ^{b)} τ_{II} is only an estimate for 510 and 410 nm excitation. Probe-wavelength dependence of vibrational relaxation time constants for processes III–V is included in the reported averages. ^{f)} Analogous τ_{III-VI} are obtained upon excitation with 340-nm 75-fs pulses.

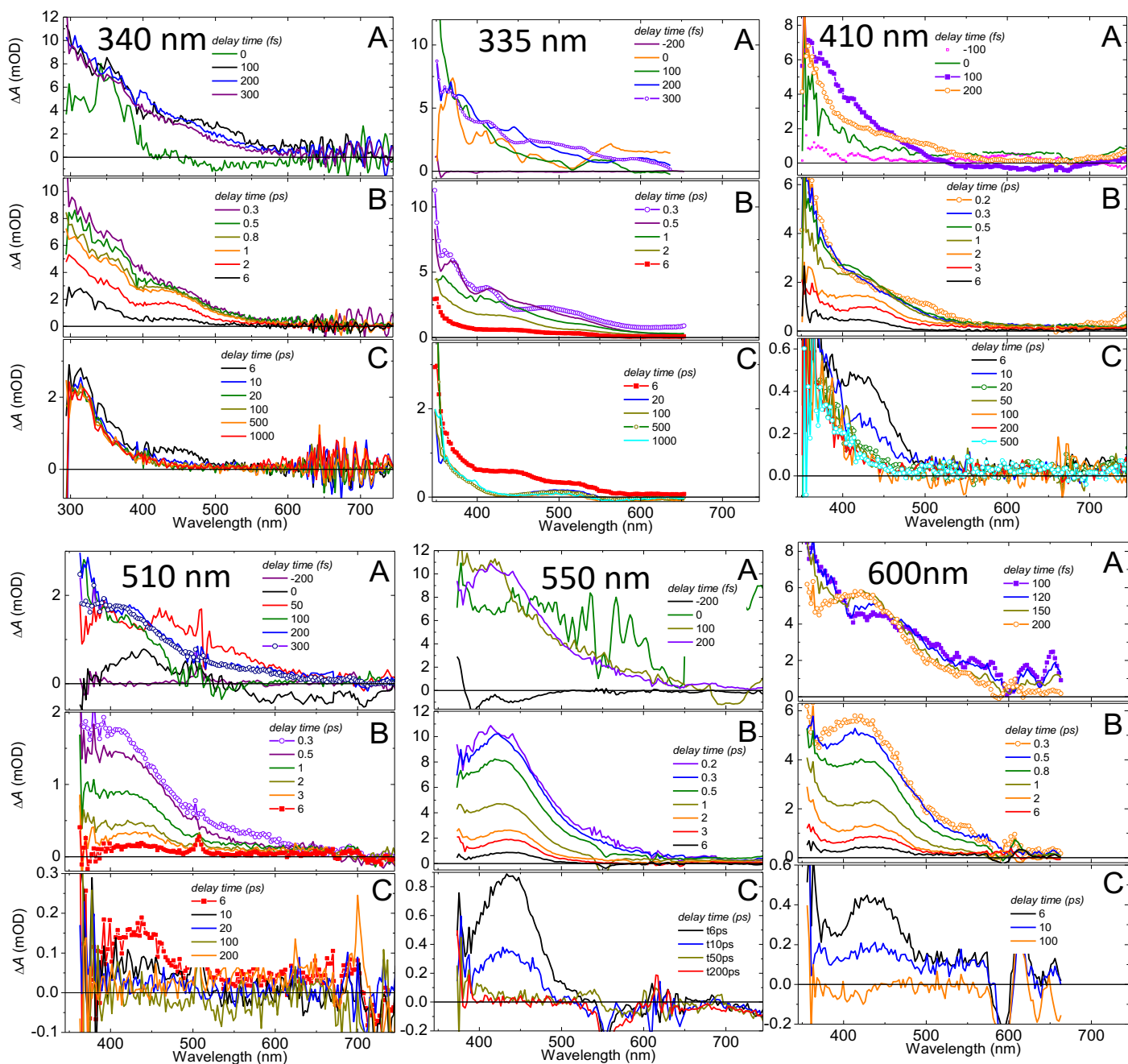


Fig. 6SI. Transient absorption spectra measured following excitation of $[\text{RuNOCl}_5]^{2-}$ at 335, 410, 510, 550, and 600 nm (335–510 nm excitation pulse duration 70 fs; 550, 600, and 675 nm excitation pulse duration 40 fs; for the 675-nm excitation ΔA spectra, see Fig. 2B, main text). Pulses in the 340 nm excitation experiment were ~ 75 fs in duration.

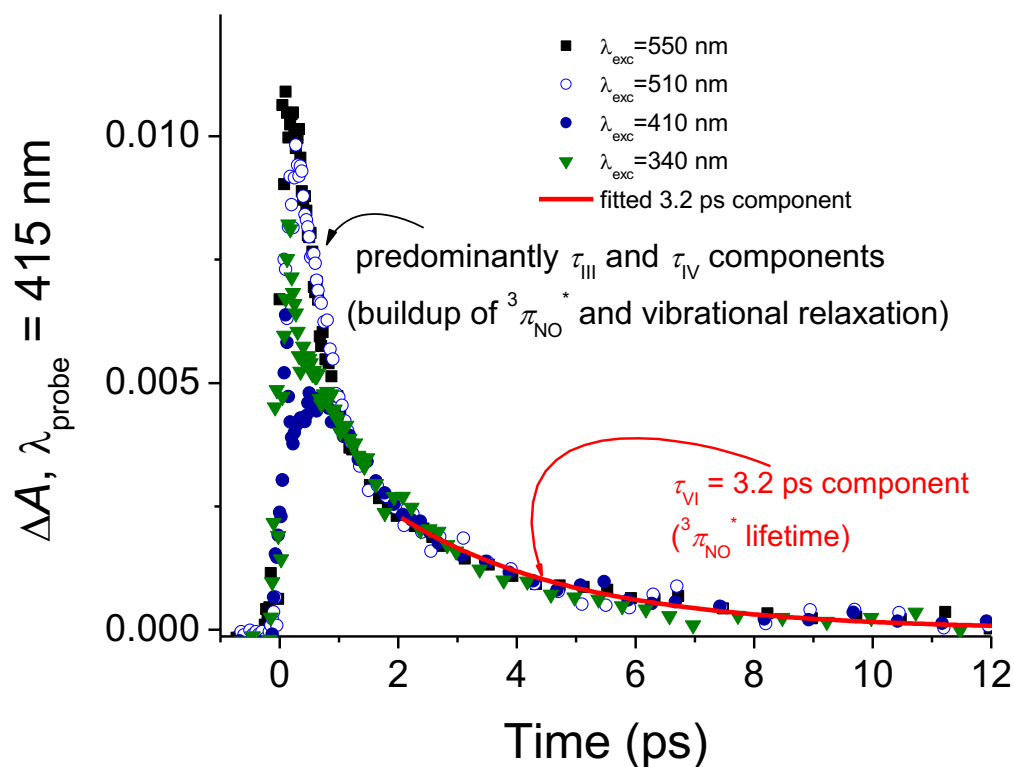


Fig. 7SI. Transient absorption kinetic traces at a 415 nm probe wavelength following excitation of $[\text{RuNOCl}_5]^{2-}$ into several excited states from 550 to 340 nm. The sub-1 ps dynamics is predominantly due to the population of the $^3\pi_{\text{NO}}^*$ state (component III in Fig. 5SI), and its vibrational relaxation (IV). The decay with a 3.2 ps time constant (fit: red line; component VI) illustrates the lifetime of the $^3\pi_{\text{NO}}^*$ state.

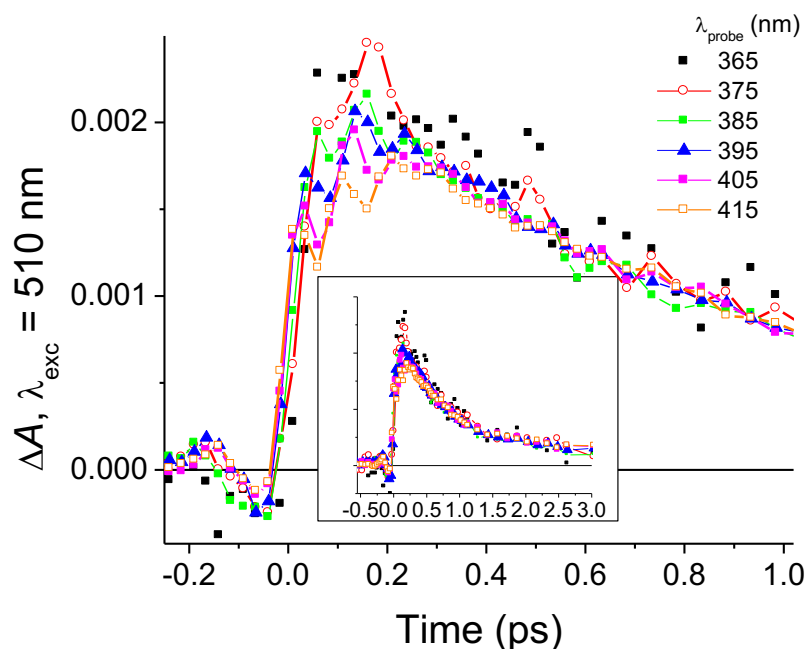


Fig. 8SI. Kinetic traces at several representative probe wavelengths following 510 nm excitation of $[\text{RuNOCl}_5]^{2-}$, illustrating a ~ 50 fs growth and a ~ 100 fs decay of hot ^1GS complexes (365–405 nm, sub-160 fs delay times, processes I and II in Fig. 5SI), and a 120-fs rise of the vibrationally coherent the $^3\pi_{\text{NO}}^*$ state (III, Fig. 5SI). The negative peak centered at -65 fs is due to the residual solvent contribution. The inset illustrates the 3.2 ps decay of the $^3\pi_{\text{NO}}^*$ state (VI, Fig. 5SI).

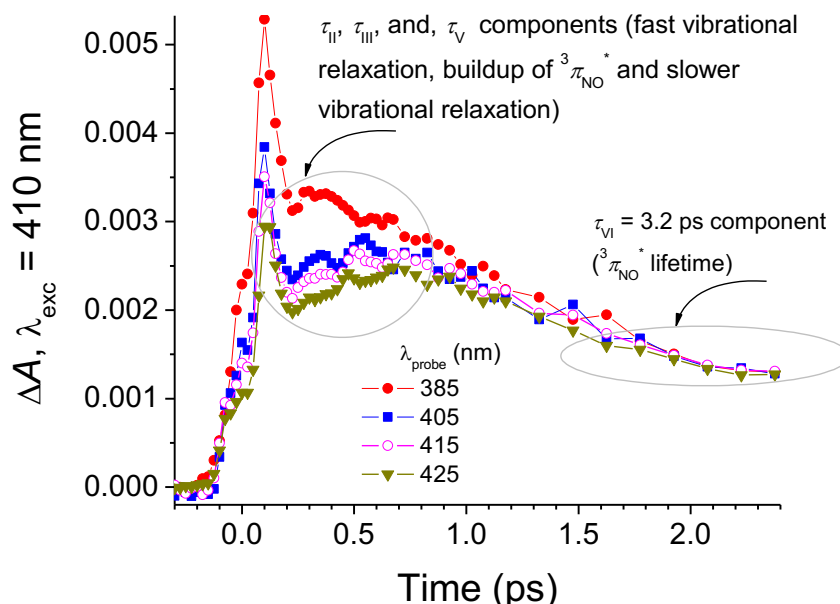


Fig. 9SI. Transient absorption kinetic traces at several representative probe wavelengths following 410 nm excitation of $[\text{RuNOCl}_5]^{2-}$, illustrating a growth and a ~ 100 fs decay of hot ^1GS complexes (processes I and II in Fig. 5SI), a 260-fs rise of the vibrationally coherent $^3\pi_{\text{NO}}^*$ state (III), and a 3.2 ps decay of the thermalized and relaxed the $^3\pi_{\text{NO}}^*$ state (VI, Fig. 5SI).

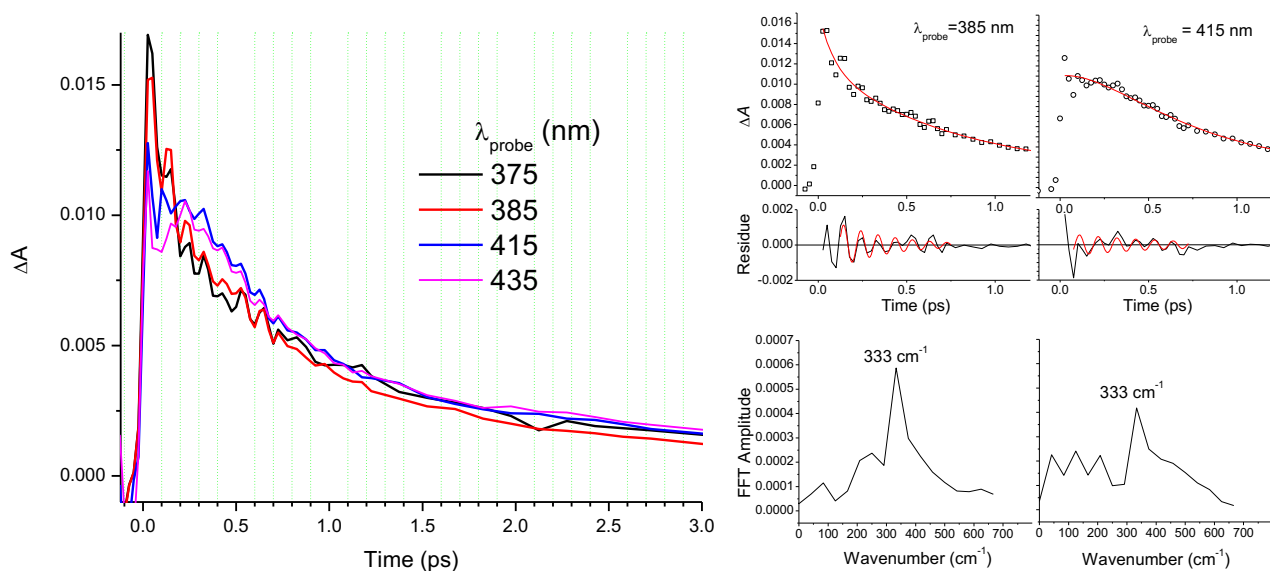


Fig. 10SI. Left: transient absorption kinetic traces measured at several representative probe wavelengths following 550-nm excitation of $[\text{RuNOCl}_5]^{2-}$, illustrating the formation of the vibrationally coherent ${}^3\pi_{NO}^*$ state and the decay of the relaxed the ${}^3\pi_{NO}^*$ state (processes III and VI in Fig. 5SI). The negative ΔA lobes between ~ -180 and -75 fs are the artefacts introduced by the subtraction of the xpm signal of the flow cell with water; this subtraction does not alter the ΔA dynamics for delay times longer than ~ -75 fs. Right, top: transient absorption kinetic traces (symbols) at the probe wavelength of 385 and 415 nm, their multiexponential fits (starting from delay times ≥ 50 fs, red), the fit residuals (black lines) and their fits (red lines) to a sum of exponentially damped cosine functions, $R(t) = \sum A_i \exp(-t/\tau_{ci}) \cos(2\pi\nu_i t + \varphi_i)$, with the amplitude (A_i), frequency (ν_i), phase (φ_i), and coherence decay time constant (τ_{ci}) set as free parameters. In these representative traces, a frequency of 333 cm^{-1} dominates with a decoherence time constant of 350 ± 120 fs, see Table 3SI for the summary. Right, bottom: fast Fourier transform (FFT) spectra of the 385 and 415 nm multiexponential fit residuals.

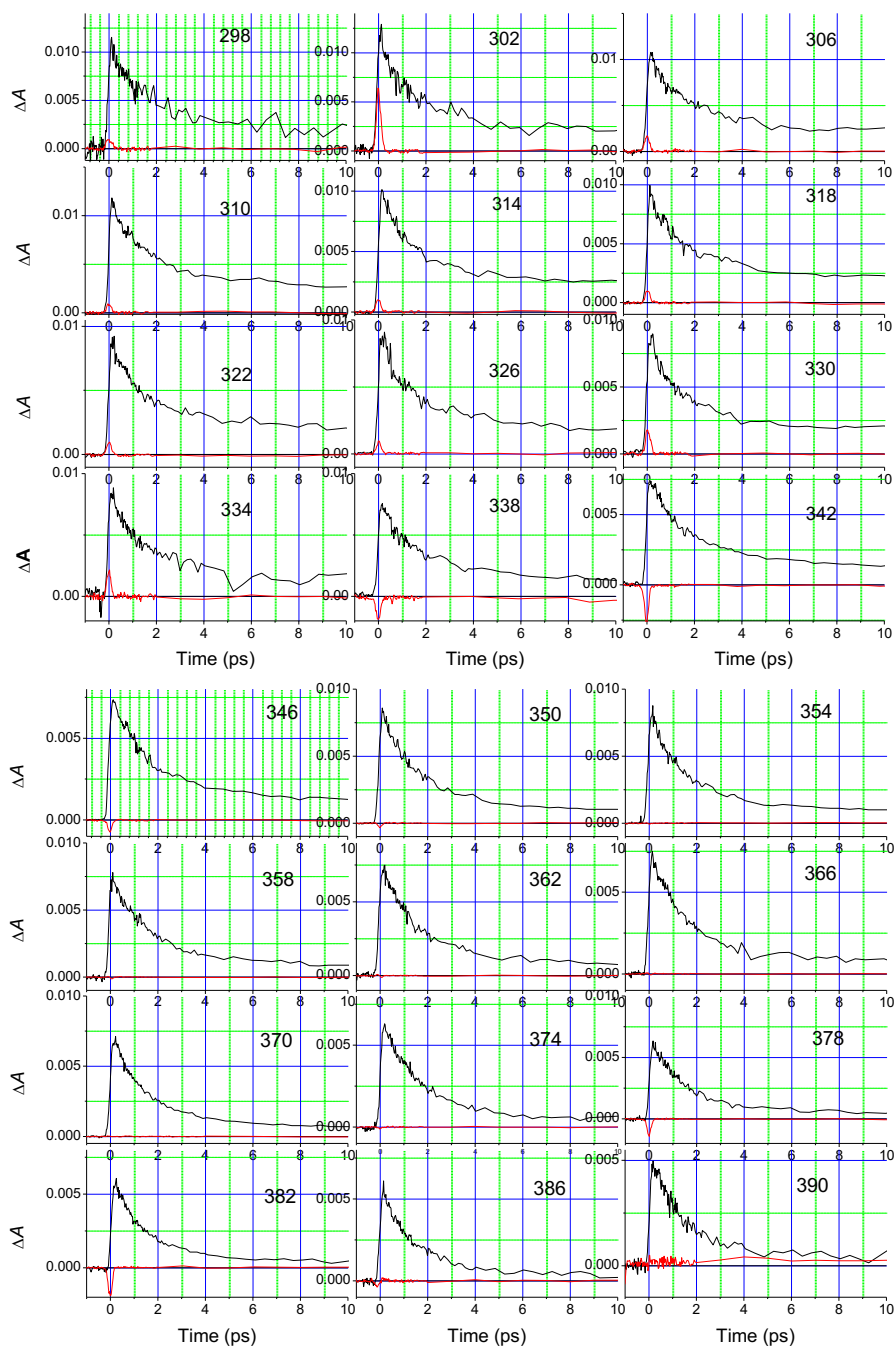


Fig. 11SI. Transient absorption kinetic traces measured in the probe region of 298–390 nm with a 4 nm wavelength increment following 340-nm 75-fs excitation of aqueous $[\text{RuNOCl}_5]^{2-}$ (black lines, probe wavelengths indicated in legends). The red curves are the ΔA kinetic traces measured for neat water under identical excitation conditions. The residual ΔA signal following a 3.2 ps decay of the $^3\pi_{NO}^*$ state (delay times longer than 8 ps) is due to the formation of a long-lived aquated product.

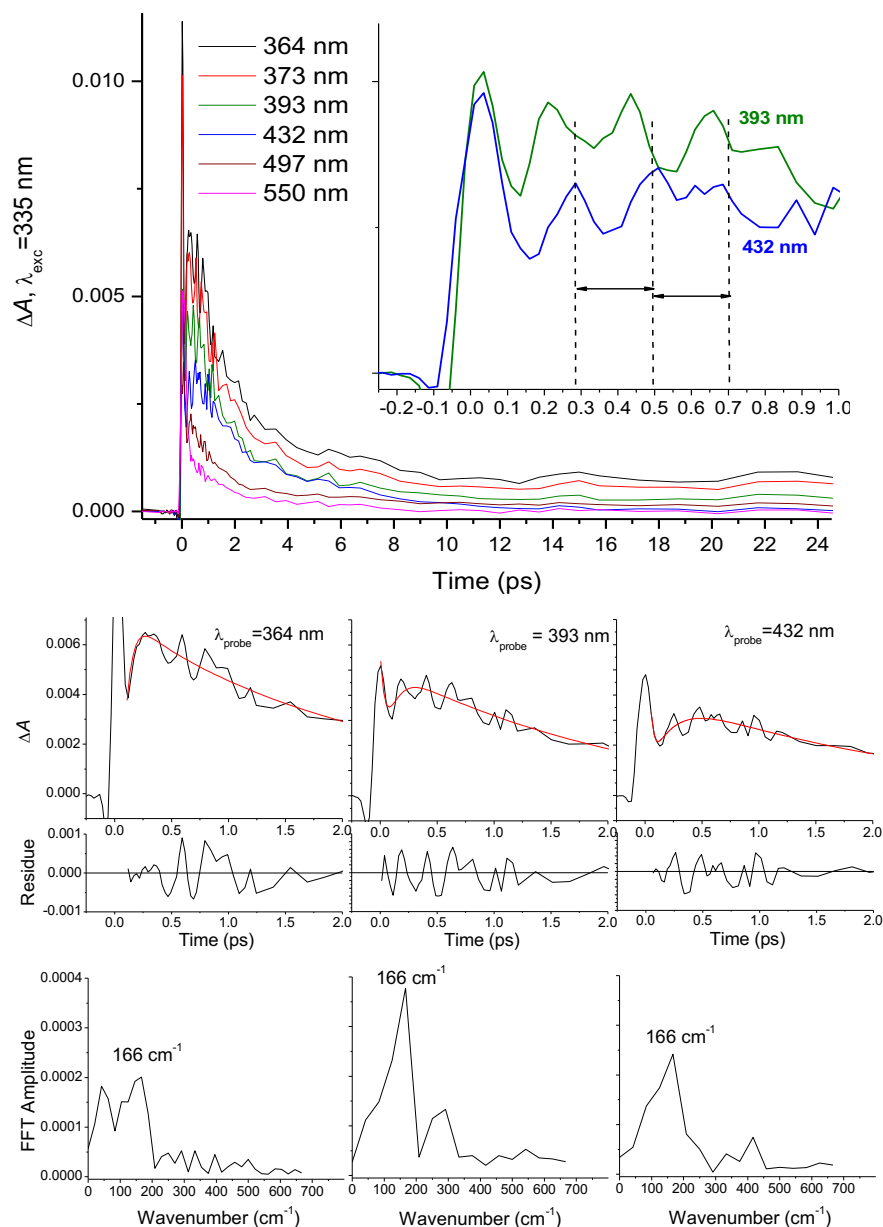


Fig. 12SI. Top: ΔA kinetic traces at several representative probe wavelengths following 335-nm excitation of aqueous $[\text{RuNOCl}_5]^{2-}$. The inset demonstrate the $\sim\pi$ shift (out-of-phase) between the oscillations detected in the blue and red wings (393 and 432-nm) of the initial $\sim 420 \text{ nm}$ band of the ${}^3\pi_{NO}^*$ product, as expected for the oscillations due to vibrational coherence in the product state. The solvent/cell xpm signals, which were not subtracted in this case, extend from ~ -120 to $\sim 120 \text{ fs}$, causing the negative $\sim -95 \text{ fs}$ lobes in the shown ΔA kinetic traces. Center and bottom: the kinetic traces at 364, 393, and 432 nm probe wavelengths (black lines), their fits to a sum of exponential decay functions (red lines), and the multiexponential fit residuals. FFT spectra of the fit residuals are shown in the bottom panel.

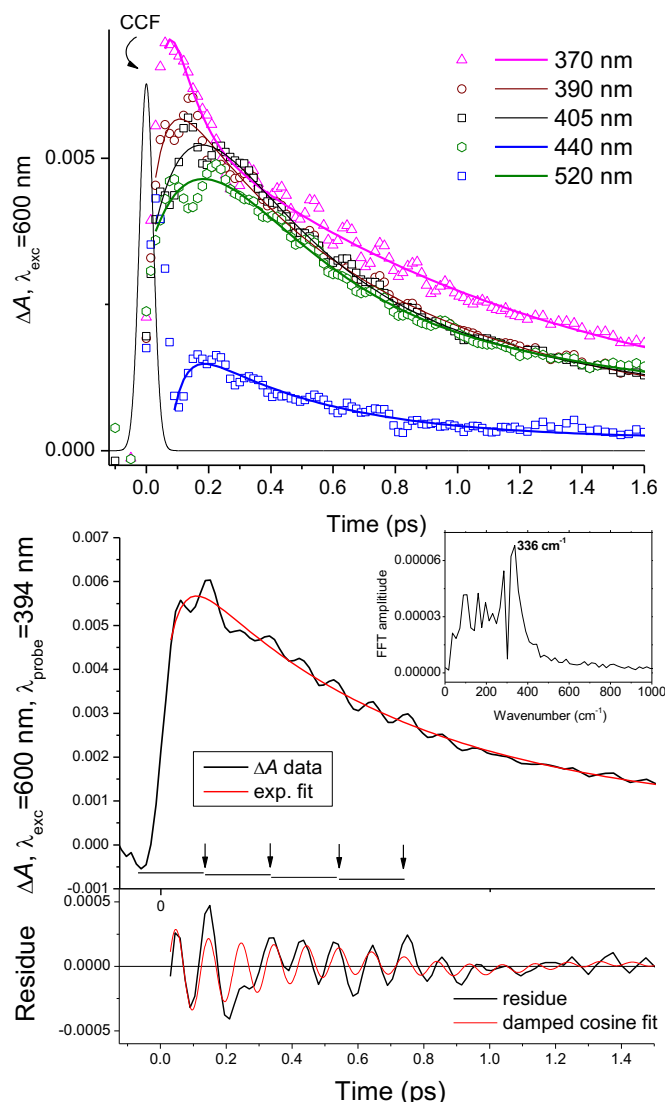


Fig. 13SI. $[\text{RuNOCl}_5]^{2-}$ excited at 600 nm. Top: the Gaussian CCF (fwhm, 45 fs) between excitation and probe pulses, ΔA kinetic traces (symbols) at several probe wavelengths and multiexponential fits (lines) illustrating the rise/decay ($\sim 50/100$ fs) of hot ^1GS (370-nm probe, processes I and II, Fig. 5SI), the rise of the vibrationally coherent $^3\pi_{NO}^*$ state (III), and the 3.2-ps $^3\pi_{NO}^*$ lifetime (VI). Bottom: a representative 394-nm ΔA kinetic trace (line), its multiexponential fit (delay times ≥ 50 fs, red), the fit residual (black lines) and its fit (red lines) to an exponentially damped cosine function (the resulting frequency and the decoherence time constants are $330 \pm 3 \text{ cm}^{-1}$ and 445 ± 107 fs). The inset shows the FFT spectrum of the fit residual. In the 394-nm ΔA trace, the negative ΔA lobe at -60 fs is the result of subtraction of the solvent/cell xpm signal; if the coherence observed is due to ISRS from the solute the ΔA lobe is expected to be positive, as shown by the time intervals which trace the oscillation maxima of the 330 cm^{-1} mode.

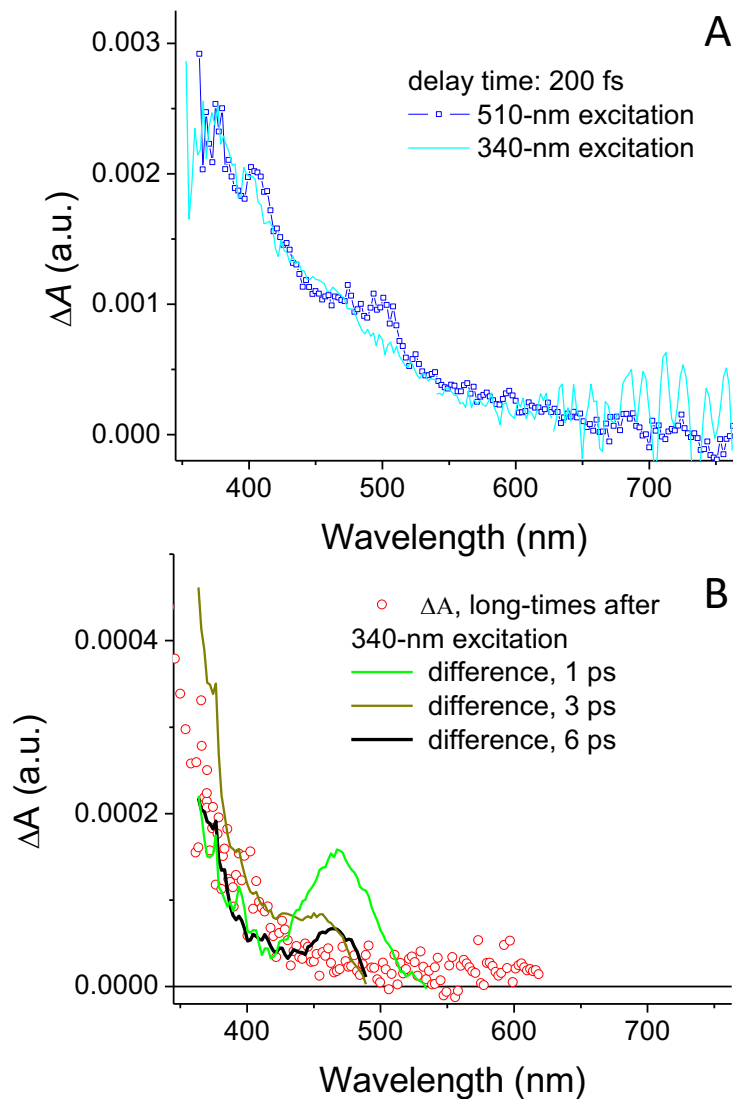


Fig. 14SI. Panel A: the 200 fs transient spectra after 340 nm excitation are similar to the ΔA spectra measured at the same delay time following 510-nm excitation. Panel B: the difference spectrum of the 340- and 510-nm ΔA spectra closely matches starting from 6 ps the long-time (≥ 100 ps) transient absorption spectra due to $[\text{Ru}(\text{H}_2\text{O})\text{Cl}_5]^{2-}$, suggesting a 2-ps time constant for the growth of this aquated product species ($3 \times \tau = \text{full growth time}$).

Table 3SI. The frequencies (ν_{1-3}) and decoherence time constants (τ_{c1-3}) of the oscillatory components in the transient absorption kinetic traces.^{a)}

λ_{exc} (nm)	1 st component		2 nd component		3 rd component	
	ν_1 (cm ⁻¹)	τ_{c1} (fs)	ν_2 (cm ⁻¹)	τ_{c2} (fs)	ν_3 (cm ⁻¹)	τ_{c3} (fs)
675	320 ± 5	~ 500	169 ± 13 ^{b)}	-	91 ± 5	~ 800
600	330 ± 3	640 ± 200	166 ± 8 ^{b)}	400 ± 70	~ 90 ^{c)}	
550	328 ± 5	350 ± 120	- ^{c)}			
510	324 ± 6	220 ± 20	- ^{c)}			
410	329 ± 6 ^{b)}	220 ± 70	142 ± 3	900 ± 100		
335	-		155 ± 6	500 ± 260		

^{a)} Obtained by subtracting the multiexponential fits from the measured ΔA kinetic traces and fitting the residue $R(t)$ to a sum of two (or, three) damped cosine functions: $R(t) = \sum A_i \exp(-t/\tau_{ci}) \cos(2\pi\nu_i t + \varphi_i)$, where A_i is the amplitude, and φ_i is the phase of the i^{th} component. ^{b)} Weak ^{c)} Very weak.

Nanosecond Transient Absorption

Nanosecond transient absorption measurements were conducted with a LP980 laser flash photolysis system (Edinburgh Instruments) using Vibrant 355-nm Nd:YAG/OPO system (OPOTEK) as the excitation source. Kinetic traces are collected with a PMT, and transient absorption spectra (as short as 20 ns delay typically) are collected with an iStar ICCD camera (Andor Technology). Samples were aqueous solutions of $[\text{RuNOCl}_5]^{2-}$ (3 mM) circulated through a 1 cm path length flow cell. Excitation was carried out at 355 nm.

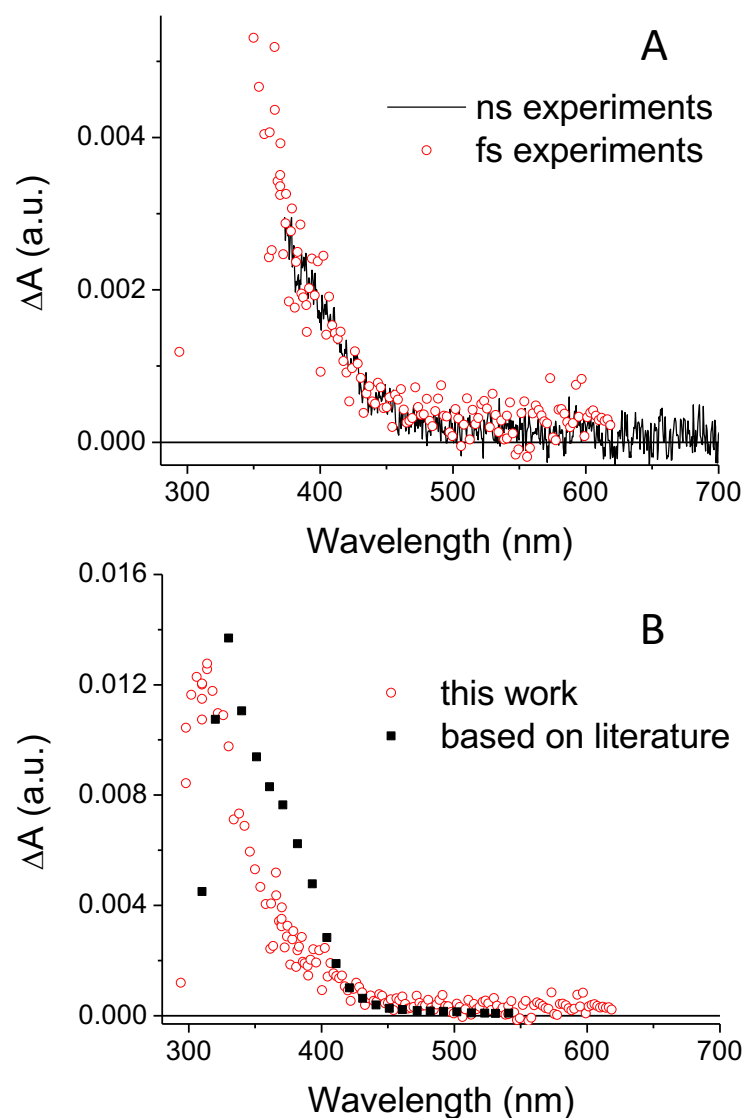


Fig. 15SI. A: the identical transient absorption spectra (delay times, 100–1000 ps) following 100-fs 340 nm excitation were averaged to increase signal-to-noise ratio and compared with the transient absorption spectrum measured at 480 ns after 335-nm nanosecond excitation. This illustrates that the long-lived photolysis product in femtosecond transient absorption experiments, assigned to be an aquated $\text{Ru}(\text{H}_2\text{O})\text{Cl}_5^{2-}$, a by-product of the NO photorelease, survives at least into a sub-microsecond time range. B: the transient absorption spectrum assigned to the formation of $\text{Ru}(\text{H}_2\text{O})\text{Cl}_5^{2-}$ does not agree with the difference spectrum, which we derived from the molecular extinction coefficient of $\text{Ru}(\text{H}_2\text{O})\text{Cl}_5^{2-}$ reported in the early work¹⁷ and the known molecular extinction coefficient of the parent complex.

Evidence for NO Photorelease upon 400 nm Irradiation

The NO photorelease from aqueous $[\text{RuNOCl}_5]^{2-}$, $[\text{RuNOCl}_5]^{2-} + h\nu \rightarrow [\text{Ru}^{\text{III}}(\text{H}_2\text{O})\text{Cl}_5]^{2-} + \text{NO}$, can be studied by observing a by-product of the NO photorelease in the reaction shown above. The formation of $[\text{Ru}^{\text{III}}(\text{H}_2\text{O})\text{Cl}_5]^{2-}$ is directly related to formation of elusive NO. By observing the ruthenium(III) complex we can infer the mechanism of NO formation and the time of its occurrence. However, the $[\text{Ru}^{\text{III}}(\text{H}_2\text{O})\text{Cl}_5]^{2-}$ photoproduct is not stable in water and undergoes rapid hydrolysis.¹⁷ A way to deal with this difficulty is to carry out the steady-state photolysis in, at least, 8 M hydrochloric acid.¹⁸ Even then, at such high concentrations of chloride ions, two ruthenium complexes are present in significant amounts: $[\text{RuCl}_6]^{3-}$ and $[\text{Ru}(\text{H}_2\text{O})\text{Cl}_5]^{2-}$, and not $[\text{Ru}(\text{H}_2\text{O})\text{Cl}_5]^{2-}$ alone. At lower chloride concentrations, the equilibrium is shifted towards the hydrolyzed complexes and, as a result, formation of several hydrolysis products becomes unavoidable in steady-state spectroscopic measurements. Fig. 16SI shows that the steady-state

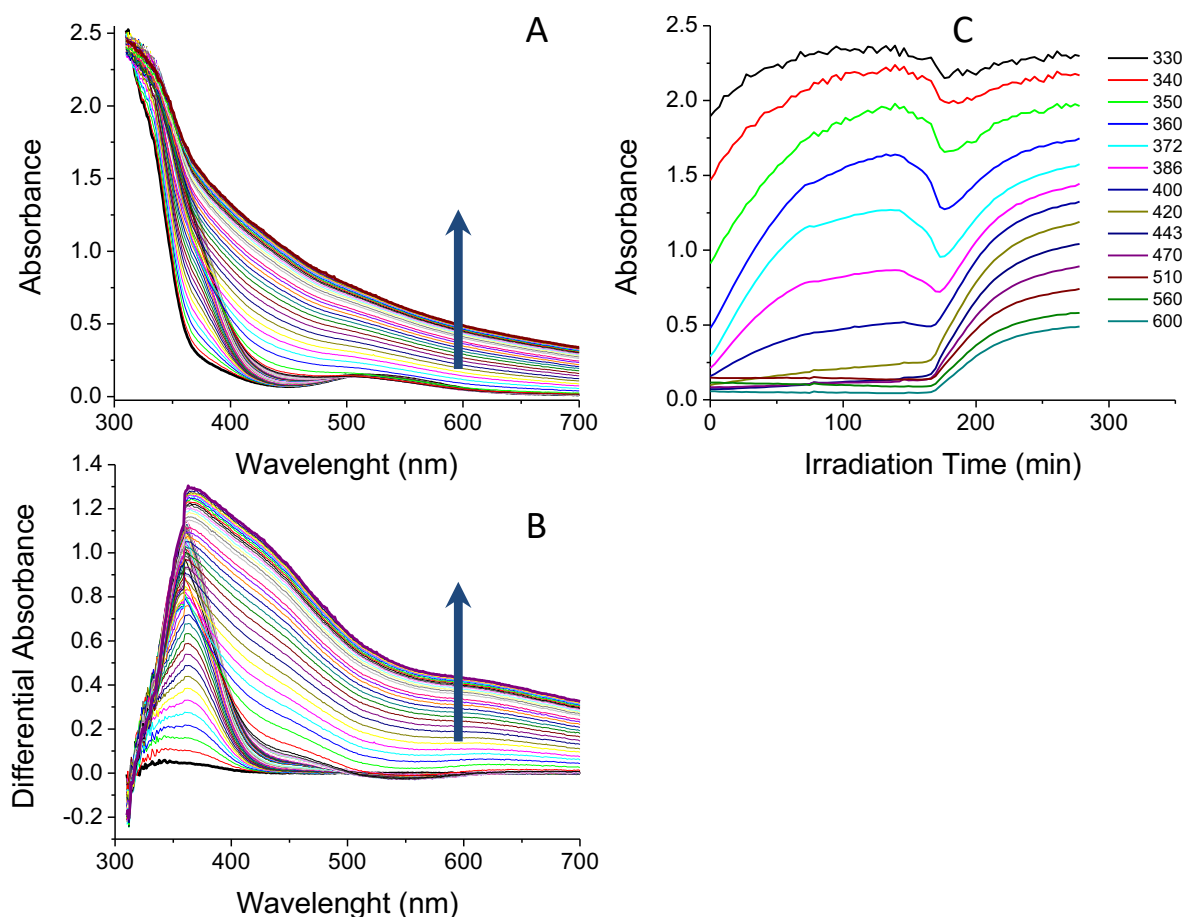


Fig. 16SI. A) Absorption spectra of aqueous solution containing 2.71 mM $\text{K}_2\text{RuNOCl}_5$ following steady-state photolysis at an irradiation wavelength of 400 nm. The initial (0

irradiation time) and final (278 min. irradiation time) spectra are shown by bold black and purple lines, respectively. B) The difference absorbance for the photolyzed and the starting solution (bold black and purple lines: 0 and 278 min. irradiation times, respectively). C) Absorption evolution at specific wavelengths shown in the legend.

photolysis (a 400-nm irradiation wavelength) is indeed complicated in dilute aqueous solutions. At the beginning of the photolysis, the absorption grows first at about 345 nm, and then, *ca.* 10 min. later this band shifts to 360 nm and continues to grow with time, as revealed by difference spectra between the absorption spectra of the initial and irradiated solutions. The shoulder at 450 nm in the difference spectra is also present. This shoulder grows with irradiation time (up to 3 hrs.), whereas the amplitude of the 360 nm band stabilizes after 1 hr., Fig. 16SI. The broad absorption across the entire visible region that occurred at the end of photolysis is due to hydrated RuO₂ nanoparticles, which are products of oxidation¹⁹ and complete hydrolysis¹⁷ of [Ru(H₂O)Cl₅]²⁻. The rate of hydrolysis increases when the oxidation state of ruthenium increases.^{17,19} Based on this, the limiting step of the RuO₂ nanoparticles formation is the oxidation of partially hydrolyzed Ru^{III} complexes. Once the oxidation to ruthenium(IV) has occurred, the nanoparticles form quickly. Thus, the steady-state 400-nm irradiation data are consistent with the NO photorelease in irradiated [RuNOCl₅]²⁻ aqueous solutions.

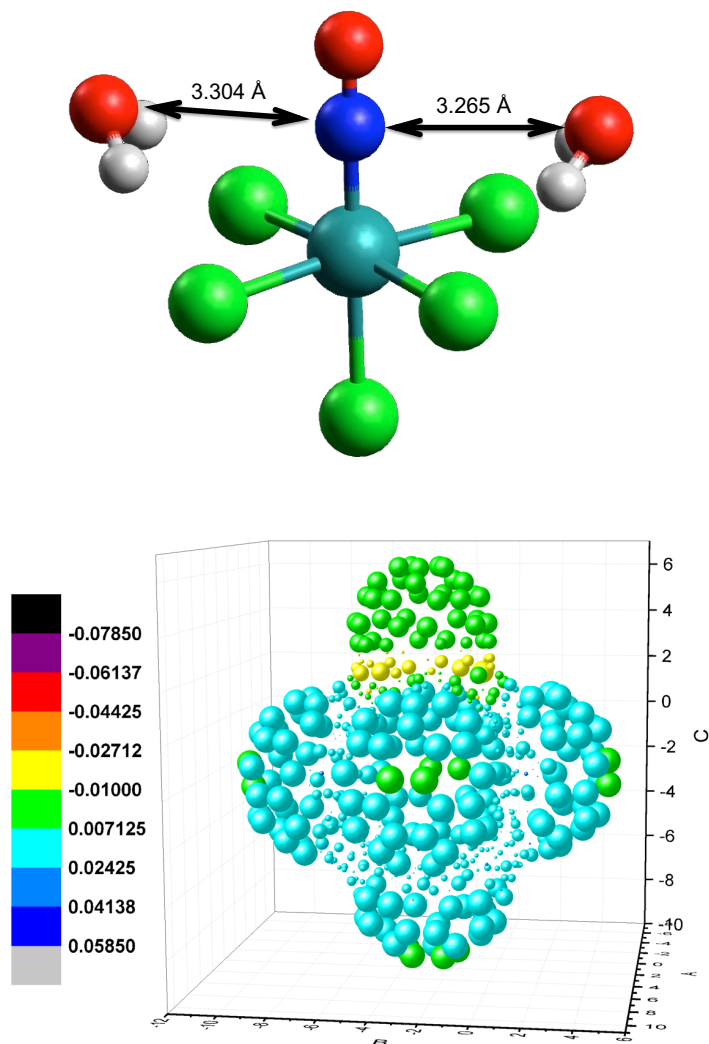


Fig. 17SI. Top: optimized geometry of $[\text{RuNOCl}_5]^{2-}$ with two explicit water molecules (VWN DFT, COSMO description of a water solvent, as implemented in ADF package). Bottom: COSMO charges of the solvation shell around $[\text{RuNOCl}_5]^{2-}$.

Table 4SI. Aqueous $[\text{RuNOCl}_5]^{2-}$ ${}^3\pi_{\text{NO}}^*$ state: numerical density functional (functional, VWN) DFT vibrational frequency calculations utilizing a TZP STO basis set with COSMO description of a water solvent, as implemented in the ADF package.

	${}^1\text{GS}$				${}^1\text{GS } 2\text{H}_2\text{O}$				${}^3\pi_{\text{NO}}^*$				${}^3\pi_{\text{NO}}^* 2\text{H}_2\text{O}$			
	cm^{-1}	f	symm.	type	cm^{-1}	f	symm.	type	cm^{-1}	f	symm.	type	cm^{-1}	f	symm.	type
1	56	0.7	e	$\partial(\text{Ru-N-O})$					60	0.07		$\rho(\text{RuNO})$	73	0.04		$\rho(\text{RuNO})$
2	60	0.7	e	$\partial(\text{Ru-N-O})$					99	7.7	e	$\partial_x(\text{Cl-Ru-Cl})$	93	1.2	e	$\partial_x(\text{Cl-Ru-Cl})$
3	110	0.01	b_1	$\partial_z(\text{Cl-Ru-Cl})$	94	0.02	b_1	$\partial_z(\text{Cl-Ru-Cl})$	100	7.3	e	$\partial_y(\text{Cl-Ru-Cl})$	104	3.4	e	$\partial_y(\text{Cl-Ru-Cl})$
4	123	0.01	b_2	$\partial_{xy}(\text{Cl-Ru-Cl})$	112	0.2	b_2	$\partial_{xy}(\text{Cl-Ru-Cl})$	110	3.7	b_1	$\partial_z(\text{Cl-Ru-Cl})$	169	0.3	b_1	$\partial_z(\text{Cl-Ru-Cl})$
5	128	0.02	e	$\partial_x(\text{Cl-Ru-Cl})$	115	0.7	e	$\partial_x(\text{Cl-Ru-Cl})$	130	0.1		$\partial(\text{Cl-Ru-N})$	119	0.5		$\partial(\text{Cl-Ru-N})$
6	129	0.01	e	$\partial_y(\text{Cl-Ru-Cl})$	117	1.0	e	$\partial_y(\text{Cl-Ru-Cl})$	138	13	e	$\partial(\text{Cl-Ru-N})$				
7	155	7.0	a_1	$\partial_z(\text{Cl-Ru-Cl})$	151	2.7	a_1	$\partial_z(\text{Cl-Ru-Cl})$	143	15	e	$\partial(\text{Cl-Ru-N})$				
8	156	0.02	e	$\partial_x(\text{Cl-Ru-Cl})$	137	1.0	e	$\partial_x(\text{Cl-Ru-Cl})$	151	0.9	b_2	$\partial_{xy}(\text{Cl-Ru-Cl})$	134	5.0	b_2	$\partial_{xy}(\text{Cl-Ru-Cl})$
9	157	0.1	e	$\partial_y(\text{Cl-Ru-Cl})$	154	0.15	e	$\partial_y(\text{Cl-Ru-Cl})$	165	0.8	a_1	$\partial_z(\text{Cl-Ru-Cl})$	161	0.14	a_1	$\partial_z(\text{Cl-Ru-Cl})$
10	275	47	a_1	$\nu(\text{Ru-Cl})$	279	33	a_1	$\nu(\text{Ru-Cl})$	240	85	a_1	$\nu(\text{Ru-Cl}_{\text{ac}})$	251	92	a_1	$\nu(\text{Ru-Cl}_{\text{ac}})$
11	284	0.04	b_1	$\nu(\text{Ru-Cl})$	281	3.0	b_1	$\nu(\text{Ru-Cl})$	241	10	b_1	$\nu(\text{Ru-Cl})$	241	1.8	b_1	$\nu(\text{Ru-Cl})$
12	317	187	e	$tr_x \nu(\text{Ru-Cl})$	314	170	e	$tr_x \nu(\text{Ru-Cl})$	281	56		$\partial(\text{Cl-Ru-N})$	278	26		$\partial(\text{Cl-Ru-N})$
13	318	175	e	$tr_y \nu(\text{Ru-Cl})$	317	167	e	$tr_y \nu(\text{Ru-Cl})$	299	209	e	as. $\nu(\text{Ru-Cl}_{\text{eq}})$	294	316	e	as. $\nu(\text{Ru-Cl}_{\text{eq}})$
14	320	50	a_1	$\nu(\text{Ru-Cl})$	325	59	a_1	$\nu(\text{Ru-Cl})$	306	307	e	as. $\nu(\text{Ru-Cl}_{\text{eq}})$	306	295	e	as. $\nu(\text{Ru-Cl}_{\text{eq}})$
15	579	4.6	e	$\partial(\text{Ru-N-O})$	570	53	e	$\partial(\text{Ru-N-O})$	317	131		sym. $\nu(\text{Ru-Cl}_{\text{eq}})$	311	107		sym. $\nu(\text{Ru-Cl}_{\text{eq}})$
16	581	4.0	e	$\partial(\text{Ru-N-O})$	577	5.0	e	$\partial(\text{Ru-N-O})$	429	21	e	$\partial(\text{Ru-N-O})$	427	19	e	$\partial(\text{Ru-N-O})$
17	620	8.3	a_1	$\nu(\text{Ru-N})$	616	38	a_1	$\nu(\text{Ru-N})$	629	2.8	a_1	$\nu(\text{Ru-N})$	628	3.8	a_1	$\nu(\text{Ru-N})$
18	1895	2249	a_1	$\nu(\text{N-O})$	1906	2091	a_1	$\nu(\text{N-O})$	1681	2188	a_1	$\nu(\text{N-O})$	1699	1974	a_1	$\nu(\text{N-O})$

Computational methodologies

The electronic transitions in the studied complex were computed at EOM-CCSD level of theory with Lanl2DZ basis set in Gaussian-09C program package. The optimized geometry for this calculation was obtained at BP86 DFT level with def2-TZVPP basis set. The initial and final electronic states for the transitions were drawn as weighted (CI expansion coefficients) sum of participating molecular orbitals.

The potential energy surfaces (PES) were constructed based on the constrained geometry optimizations with fixed ruthenium/nitrogen distance and ruthenium/nitrogen/oxygen angle. The constrained geometry optimizations were carried out with help of VWN DFT functional, TZP basis set, and COSMO solvating model in the ADF program package. The singlet or triplet nature of the spin state was specified for the singlet PES and triplet PES in the input files.

The vibrational frequencies were computed numerically (ADF, VWN functional, TZP basis set) to take in account solvation implicitly in terms of COSMO model. The results were compared to the numerical vibrational frequencies with two explicit water molecules added. In both cases, the geometries were optimized prior to frequencies calculations. The solvation shell around the studied solute was shown as colored spheres (Fig. 17SI), where the spheres' color depends on the charge placed by the COSMO model at specific coordinates and the size of the sphere is proportional to the surface area of the element. The computational results are presented in Fig. 1,2, and 17SI and Table 1 and 4SI, and the references to the methodologies used are given in the Figure and Table captions.

References

1. Emel'yanov, V. A.; Fedotov, M. A.; Belyaev, A. V.; Tkachev, S. V. A Multinuclear Magnetic Resonance Study of Transformations of Ruthenium(II) Nitrosyl Chloride Complexes in Aqueous Solutions. *Russ. J. Inorg. Chem.* **2013**, *58*, 956–963, DOI: 10.1134/S003602361308007X
2. Durig, J. R.; McAllister, W. A.; Willis Jr, J. N.; Mercer, E. E. Far Infrared Spectra of Potassium and Ammonium Pentahalonitrosylruthenates. *Spectrochim. Acta* **1966**, *22*, 1091–1100, DOI: 10.1016/0371-1951(66)80199-6
3. Tosi, L. The Polarized Raman and Infrared Spectra of $K_2[RuCl_5NO]$. *J. Raman Spectrosc.* **1977**, *6*, 20–25, DOI: 10.1002/jrs.1250060106
4. Khodashova, T. S.; Bokii, B. Structure of Potassium Nitroso-Pentachlororuthenate. *J. Struct. Chem.* **1960**, *1*, 138–145, DOI: 10.1007/BF00738930
5. Baranovskii, V. I.; Mal'tsev, D. A.; Sizova, O. V. Excited-State Potential Surfaces of Ruthenium Nitrosyl Complexes: Conical Intersections and the Jahn-Teller Effect. *Russ. Chem. Bull., Int. Ed.*, **2012**, *61*, 973–979, DOI: 10.1007/s11172-012-0140-4
6. Bottomley, F. Nitrosyl Complexes of Ruthenium. *Coord. Chem. Rev.*, **1978**, *26*, 7–32, DOI: 10.1016/S0010-8545(00)82063-9
7. Perdew, J. P. Density-Functional Approximation for the Correlation Energy of the Inhomogeneous Electron Gas. *Phys. Rev. B*: **1986**, *33*, 8822–8824, DOI: 10.1103/PhysRevB.33.8822
8. Becke, A. D. Density-Functional Thermochemistry. III. The Role of Exact Exchange. *J. Chem. Phys.*, **1993**, *98*, 5648–5652, DOI: 10.1063/1.464913
9. Weigend, F.; Ahlrichs, R. Balanced Basis Sets of Split Valence, Triple Zeta Valence and Quadruple Zeta Valence Quality for H to Rn: Design and Assessment of Accuracy. *Phys. Chem. Chem. Phys.* **2005**, *7*, 3297–3305, DOI: 10.1039/B508541A
10. Eichkorn, K.; Weigend, F.; Treutler O.; Ahlrichs, R. Auxiliary Basis Sets for Main Row Atoms and Transition Metals and Their Use to Approximate Coulomb Potentials. *Theor. Chem. Acc.*, **1997**, *97*, 119–124, DOI: 10.1007/s002140050244
11. Pal, S. K.; Mereshchenko, A. S.; Butaeva, E. V.; El-Khoury, P. Z.; Tarnovsky, A. N. Global Sampling of the Photochemical Reaction Paths of Bromoform by Ultrafast Deep-UV through Near-IR Transient Absorption and Ab Initio Multiconfigurational Calculations. *J. Chem. Phys.*, **2013**, *138*, 124501, DOI: 10.1063/1.4789268

12. Panov, M. S.; Voskresenska, V. D.; Ryazantsev, M. N.; Tarnovsky, A. N.; Wilson, R. M. 5-Azido-2-Aminopyridine, a New Nitrene/Nitrenium Ion Photoaffinity Labeling Agent that Exhibits Reversible Intersystem Crossing Between Singlet and Triplet Nitrenes. *J. Am. Chem. Soc.*, **2013**, *135*, 19167–19179, DOI: 10.1021/ja405637b
13. Kovalenko, S. A.; Ernsting N.; Ruthmann, J. Femtosecond Hole-Burning Spectroscopy of the Dye DCM in Solution: the Transition from the Locally Excited to a Charge-Transfer State. *Chem. Phys. Lett.* **1996**, *258*, 445-454, DOI: 10.1016/0009-2614(96)00647-1
14. Kovalenko, S. A.; Dobryakov, A. L.; Ruthmann, J.; Ernsting, N. P. Femtosecond Spectroscopy of Condensed Phases with Chirped Supercontinuum Probing. *Phys. Rev.*, **1999**, *A 59*, 2369–2384, DOI: 10.1103/PhysRevA.59.2369
15. Rasmusson, M.; Tarnovsky, A. N.; Åkesson, E.; Sundström, V. On the use of Two-Photon Absorption for Determination of Femtosecond Pump-Probe Cross-Correlation Functions. *Chem. Phys. Lett.* **2001**, *335*, 201–208, DOI: 10.1016/S0009-2614(01)00057-4
16. Ekvall, K.; van der Meulen, P.; Dhollande, C.; Berg, L.-E.; Pommeret, S.; Naskreski, R.; Mialocq, J.-C. Cross Phase Modulation Artifact in Liquid Phase Transient Absorption Spectroscopy. *J. Appl. Phys.* **2000**, *87*, 2340–2352, DOI: 10.1063/1.372185
17. Fine, D. A. Chloride Complexes of Ruthenium (III). Ph.D. Thesis, University of California, **1960**, <https://escholarship.org/uc/item/5161r7m6>
18. Cox, A. B.; Wallace, R. M. Photolysis of Nitrosylruthenium Chloro Complexes. *Inorg. Nucl. Chem. Lett.* **1971**, *7*, 1191–1194, DOI: 10.1016/0020-1650(71)80064-8
19. Leroy, A. F.; Morris, J. C. The Kinetics of Hydrolysis of Rutheniumnitrosyltrichloride. *J. Inorg. Nucl. Chem.* **1971**, *33*, 3437–3453, DOI: 10.1016/0022-1902(71)80666-8